ACS Catalysis

pubs.acs.org/acscatalysis Research Article

Selectively Reducing Nitrate into NH_3 in Neutral Media by PdCu Single-Atom Alloy Electrocatalysis

Cheng Du,[#] Siyan Lu,[#] Jia-ao Wang,[#] Xiyang Wang, Maoyu Wang, Holly M. Fruehwald, Lei Wang, Baizhou Zhang, Tao Guo, Joel P. Mills, Wei Wei, Zuolong Chen, Youchao Teng, Jingyan Zhang, Cheng-Jun Sun, Hua Zhou, Rodney D. L. Smith, Brian Kendall, Graeme Henkelman, and Yimin A. Wu*

Cite This: *ACS Catal.* 2023, 13, 10560−10569 Read Online

ACCESS | Metrics & More | Article Recommendations | Supporting Information

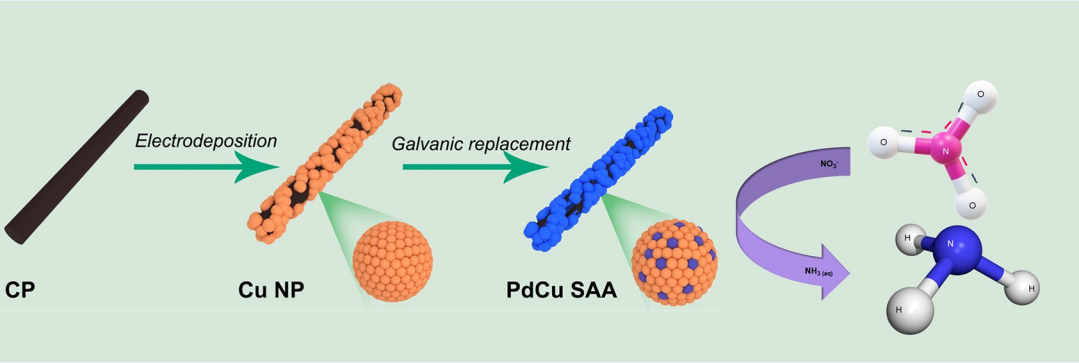

ABSTRACT: Electrocatalytic nitrate reduction reaction (NO_3^-RR) technology provides a promising solution to recover the nitrate nutrition from wastewater through catalyzing nitrate reduction into value-added NH_3. However, the selectivity and efficiency of electrocatalysts are frustrated due to the imbalance of *H adsorption (for NO_3 hydrogenation) and unavoidable adjacent *H self-coupling on active sites, resulting in competitive hydrogen evolution reaction (HER). Here, we report a PdCu single-atom alloy (SAA) catalyst that allows isolated Pd sites to produce *H for the hydrogenation process of $*NO_3$ on neighboring Cu sites, which can restrain the *H self-coupling through extending the distance between two *H and thus effectively suppress competitive HER. Consequently, the PdCu SAA catalyst exhibits an ultrahigh NH_3 Faraday efficiency (FE) of 97.1% with a yield of 15.4 μmol cm^{-2} h^{-1} from the electrocatalytic NO_3^-RR in the neutral electrolyte, outperforming most of the reported catalysts. Single-crystal experiments and theoretical calculations further prove that the introduction of atomic Pd on the Cu (100) surface could serve as the main active site and greatly decrease the energy barrier of the rate-determining step (RDS) on Cu from ΔG = 0.39 eV (*NOO → *NOOH) to ΔG = 0.10 eV of *NOH → *NHOH on PdCu SAA.

KEYWORDS: *wastewater treatment, NH_3 synthesis, nitrate reduction, single-atom alloy, electrocatalysis*

INTRODUCTION

With the rapid development of modern industry and agriculture, nitrate waste from industrial sewage and over-fertilization has caused serious pollution in the biosphere and water bodies, which is threatening human health and ecological safety.[1,2] Currently, the removal of nitrate waste in wastewater mainly relies on biological, physical, and chemical treatments, such as bacterial denitrification, ion exchange, and reverse osmosis.[2] Nevertheless, those traditional methods are severely limited by rigorous operation conditions, high cost of posttreatment, and tedious procedures.[2] To circumvent these problems, newly developed electrocatalytic nitrate reduction reaction (NO_3^-RR) technology driven by green electric energy has been developed to recover nutrition flexibly and effectively from nitrate in wastewater, by catalyzing aqueous nitrate reduction into N_2 (main product) and NH_3 (by-product) under ambient temperature and pressure.[3−5] Although promising, the accessibility of such electrocatalytic technology in the industrial treatment of nitrate waste still suffers from an intractable limitation, specifically that the main product N_2 possesses very limited economic value and is difficult to be reused.[6−8] Moreover, the competitive hydrogen evolution reaction (HER) over the electrocatalyst draws electrons from the nitrate reduction processes, resulting in a low Faraday efficiency (FE) of electrocatalytic NO_3^-RR.[1,9] Although

Received: March 9, 2023
Revised: July 10, 2023

https://doi.org/10.1021/acscatal.3c01088
ACS Catal. 2023, 13, 10560−10569

alkaline electrolytes can suppress HER for selective NO_3^-RR, their strong corrosivity to reactors would severely increase the economic cost of large-scale industrial applications.[10−12] Therefore, an emerging electrocatalyst is urgently needed to catalyze nitrate reduction selectively and effectively into value-added NH_3 under mild neutral media to increase the economic value of this process, since NH_3 is an important precursor to producing fertilizer and urea for agriculture.

To generate NH_3 from NO_3^-RR, NO_3^- is typically adsorbed on the surface of the electrocatalyst and then goes through a series of hydrogenation steps.[2,13] Recently, Cu has been found to have promising nitrate reduction performance due to its excellent *NO_3 adsorption ability.[14−16] However, too weak *H adsorption on Cu limits the following hydrogenation steps, resulting in low catalytic performance. To meet this challenge, enormous effort has been devoted to introducing an additional *H adsorption site in the Cu-based catalyst. For instance, CuNi and CuPd catalysts have been developed for promoting nitrate reduction, due to the outstanding *H generation ability of those second elements.[17−20] However, the *H produced on those introduced *H adsorption sites may cross-couple and desorb through the Tafel step, which cannot suppress HER well and promote NO_3^-RR.[21]

To avoid the possibility of HER from the *H intercoupling, in this work, we design a PdCu single-atom alloy (SAA) with atomic Pd atoms on the surface of Cu nanoparticles. Due to the isolated position of Pd atoms, the produced *H on Pd sites are separated and hard to intercouple, thus limiting the HER. As a result, the PdCu SAAs exhibit ultrahigh selectivity with an FE of 97.1%, accompanied by a NH_3 generation rate of 15.4 μmol cm^{-2} h^{-1}. To further investigate the catalytic active sites and reaction mechanism, a model PdCu SAA was experimentally prepared using a Cu single crystal with different crystal faces and tested for NO_3^-RR. Combined with density functional theory (DFT) calculations, we conclude that atomically dispersed Pd atoms on Cu (100) are the most active catalytic sites, which can decrease the energy barrier of the rate-determining step (RDS) and promote NO_3^-RR.

Synthesis and STEM Characterizations. A PdCu SAA was prepared through the spontaneous galvanic replacement reaction, which was driven by the reduction potential difference between Na_2PdCl_4 and Cu.[22,23] As schematically shown in Figure 1A, Cu nanoparticles were first electrodeposited on a carbon paper (CP) substrate and then immersed into extremely dilute 0.1 mg mL^{-1} Na_2PdCl_4 ethylene glycol solution for 15 min under 80 °C (for experimental details, please see the Supplementary Information). Here, ethylene glycol serves as solvent for the reaction, due to its mild reduction ability to prevent the possible oxidation of Cu. As seen from the scanning electron microscopy (SEM) images (Figure S1), no obvious change was observed in the morphology of Cu after its galvanic replacement reaction with Na_2PdCl_4. However, compared to the pure Cu sample, many bright atoms can be found from the PdCu SAA in the darker lattice from the aberration-corrected high-angle annular dark-field scanning transmission electron microscopy (AC-HAADF-STEM) images (Figure 1B−D and Figure S2). Based on the *Z*-contrast difference between Cu and Pd atoms, the darker contrast belongs to the Cu lattice while the brighter contrast is the Pd atoms, as marked by the arrows (Figure 1C,D). Those AC-HAADF-STEM images directly demonstrate the atomic dispersion of Pd atoms in the PdCu SAA. Scanning transmission electron microscopy (STEM) and

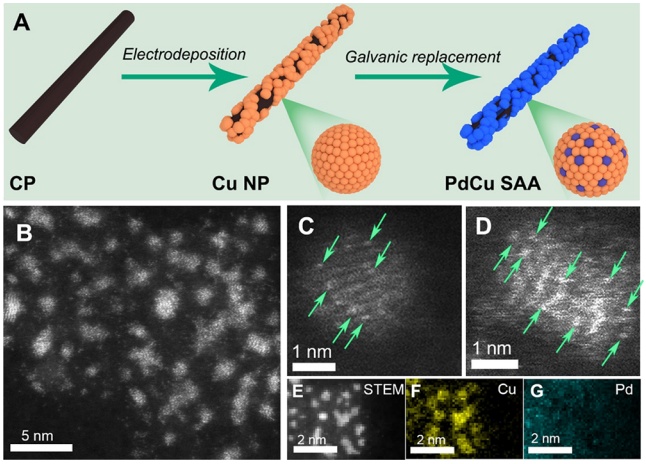

Figure 1. Synthesis and STEM characterization. (A) Schematic illustration of the synthesis of PdCu SAA. (B) AC-HAADF-STEM image of PdCu SAA. (C, D) Enlarged AC-HAADF-STEM images of PdCu SAA. (E) STEM image of PdCu SAA. (F, G) STEM-EDS mapping of Cu and Pd elements in PdCu SAA.

energy-dispersive X-ray spectroscopy (EDX) mapping further prove the co-existence of the Pd and Cu elements in the PdCu SAA (Figure 1E−G). The STEM-EDX mapping image of the Pd signal looks relatively weak, due to its extremely low content of 0.1 wt %, as determined by the inductively coupled plasma mass spectrometry (ICP-MS) analysis. EDX cannot be used to quantify the amount of single atoms (Figure S3). EDX STEM can analyze the homogeneity of chemical composition of materials at low magnification. However, at the atomic scale, the complex electron scattering between the number of X-rays detected and the number of atoms the probe interacts with makes it impossible to directly relate X-ray counts to the number or density of atoms.[24,25]

Structural Characterization and Bader Charge Analysis. To study the crystal structure, grazing incidence X-ray diffraction (GI-XRD) test was conducted for both the PdCu SAA and Cu samples. Both samples show obvious diffraction peaks of Cu (111) (200) and (220) planes (Figure 2A). No Pd peak appeared in the GI-XRD spectrum of PdCu SAA, indicating that no Pd crystalline phase formed in the sample, which agrees with the AC-HAADF-STEM results. Core-level X-ray absorption spectroscopy (XAS) was further performed to study the local coordination structure of Pd and Cu in PdCu SAA. As shown in the Pd K-edge X-ray absorption near-edge structure (XANES) and the extended X-ray absorption fine structure (EXAFS) (Figure 2B), the white line of PdCu SAA shows a slight shift to lower energy for the adsorption edge (E_0) compared to that of Pd foil, indicating that Pd in PdCu SAA has a charge transfer with Cu support and carries a negative charge. The Bader charge analysis of PdCu SAA with Cu (100) reveals that the isolated Pd atoms carry substantially negative charges (Figure 2C), confirming the experimental observations. Moreover, the Fourier transform (FT) of the k^3-weighted EXAFS curve of the Pd K-edge of PdCu SAA shows only one main peak at 2.1 Å, indicating that the Pd atoms possess only one coordination (Pd−Cu), which is different from the Pd−Pd coordination in Pd foil at 2.4 Å (Figure 2D, Figure S4, and Table S1). These results indicate that the Pd exists in PdCu SAA in single-atom form with Pd−Cu local coordination.[26,27] In addition, high-resolution wavelet-transform EXAFS (WT-EXAFS) in k and R spaces were also

https://doi.org/10.1021/acscatal.3c01088
ACS Catal. 2023, 13, 10560−10569

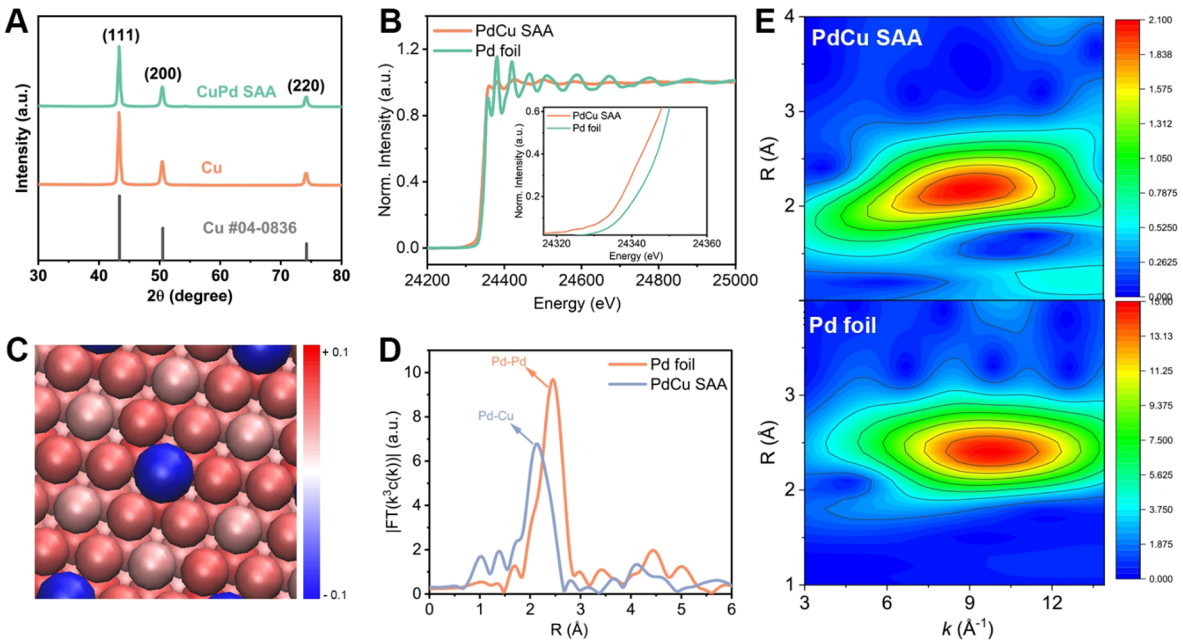

Figure 2. Structural characterization and Bader charge analysis. (A) GIXRD spectra of PdCu SAA and Cu. (B) Pd L-edge XANES and EXAFS of PdCu SAA and Pd foil reference; the inset image is the enlarged spectra. (C) Bader charge analysis of PdCu SAA with Cu (100); the red sphere represents Cu, and the blue sphere represents Pd atoms. (D) Pd L-edge Fourier-transform EXAFS spectra of PdCu SAA and Pd foil reference. (E) Wavelet transforms for the k^3-weighted EXAFS signals of PdCu SAA and Pd foil reference.

presented to reveal the dispersion state of Pd atoms in PdCu SAA and Pd foil (Figure 2E). The WT-EXAFS oscillations show the main peak at about 8.9 $Å^{-1}$, which can be attributed to the Pd−Cu coordination for PdCu SAA, while the main peak at around 9.8 $Å^{-1}$ belongs to the Pd−Pd coordination in Pd foil. Combined with the EXAFS analysis and AC-HAADF-STEM images, the single-atom dispersion of Pd atoms in the PdCu SAA could be synergistically confirmed.

Electrocatalytic Nitrate Reduction. To evaluate the electrocatalytic NO_3^-RR performance of the PdCu SAA, linear sweep voltammetry (LSV) was first measured in an H-cell with 0.5 M Na_2SO_4 as the neutral electrolyte (Methods). The current density of PdCu SAA greatly increased after the addition of 600 ppm NO_3^-, indicating its high activity toward NO_3^-RR (Figure S5). To further quantify the activity of electrocatalytic NO_3^-RR, chronoamperometry was measured for NO_3^-RR under different applied potentials and the produced ammonia was confirmed by both UV−visible (UV−vis) and nuclear magnetic resonance spectroscopy (NMR) (Figure S6). Given the high solubility of NH_3 in water, the electrolyte after electrolysis was taken out and measured to quantify the NH_3 production. Indophenol blue colorimetry was first adopted to quantify the NH_3 concentration in the electrolyte with the assistance of UV−vis spectroscopy (Figure S7A,B). The yields of both PdCu SAA and Cu increased with the increase of applied negative potentials (Figure 3A), while the FE reached a maximum at −0.6 V (Figure 3B). Specifically, the PdCu SAA exhibits the highest FE of 97.1% with a yield of 15.4 μmol cm^{-2} h^{-1} under −0.6 V, which is much better than that of Cu (FE of 81.2% with a yield of 11.0 μmol cm^{-2} h^{-1}) (Figure 3B). Specifically, the selectivity of this work outperforms most of the reported NO_3^-RR electrocatalysts in the neutral electrolyte (Table S2). To make a cross-verification of the performance of the PdCu SAA, NMR was used to determine the NH_3 production. PdCu SAA and Cu show a similar performance-potential trend, namely, that yield increases with the increasing applied potential while FE reaches a maximum at −0.6 V (Figure 3C,D, Figure S6C,F). In detail, the highest FE for PdCu SAA is 94.9% with a yield of 12.1 μmol cm^{-2} h^{-1}, which is still much better than that of Cu (FE of 71.7% with a yield of 9.7 μmol cm^{-2} h^{-1}) based on the NMR quantification method. Considering the possible influence of NH_3 from the atmospheric environment and confirming the source of nitrogen in the reaction, a ^{15}N isotope experiment was also conducted with a $Na^{15}NO_3$ feed to confirm the source of NH_3 production (Figure 3E,F). The electrolyte after electrolysis of $Na^{15}NO_3$ shows the apparent doublet peaks in the range of 7.2 to 6.8 ppm, which is due to H atoms binding to ^{15}N atoms with spin−spin coupling. In contrast, $Na^{14}NO_3$ electrolysis produces triplet peaks due to the symmetric distribution of H atoms binding with ^{14}N atoms (Figure 3E). Besides this qualitative evidence, it is also worth noting that the PdCu SAA shows a very similar FE value (92.3%) in $Na^{15}NO_3$ electrolysis compared to that of $Na^{14}NO_3$ electrolysis (97.1%) (Figure 3F). The PdCu SAA also shows good stability, maintaining an FE above 95% during a 10 h test (Figure S8). We also measured the FE and yield of NO_2^- (Methods, Figure S9). The PdCu SAA shows a lower FE and yield of converting NO_3^- to NO_2^- compared with Cu (Figure S9). This is consistent with the high FE of converting NO_3^- to NN_3 using PdCu SAA (Figure 3).

In order to investigate the effect of the amount of Pd loading, we synthesized PdCu alloy NP and Pd NP on Cu through increasing the Pd content (Methods). XRD patterns show that the formation of Pd−Pd and Pd−Cu bonds was observed with the increasing of Pd loading (Figure S10). Although the NH_3 yield increased after the increase of Pd content in the PdCu materials, the FE apparently decreased (Figure S11). These results indicate that the highly atomic dispersion of Pd in the Cu nanoparticles is necessary for high NH_3 selectivity. What should be noted is that Pd is an

https://doi.org/10.1021/acscatal.3c01088
ACS Catal. 2023, 13, 10560−10569

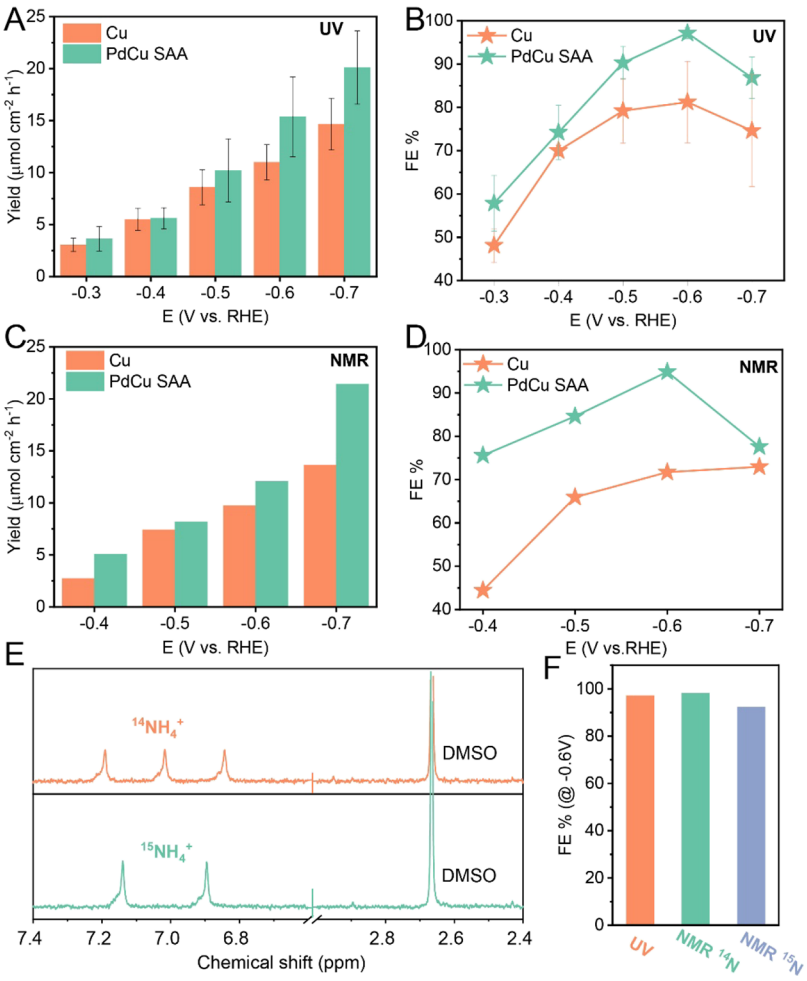

Figure 3. Electrocatalytic nitrate reduction performance characterizations. (A, B) Yield (A) and FE (B) results of PdCu SAA and Cu based on the UV detection method for NH_3. (C, D) Yield (C) and FE (D) results of PdCu SAA and Cu based on the NMR detection method for NH_3. (E) NMR spectra of produced NH_3 from $^{14}NO_3^-$ and $^{15}NO_3^-$ feeding. (F) Comparison of FE from different NH_3 detection methods under −0.6 V over PdCu SAA.

expensive noble metal, whose high content may increase the total cost of the catalyst. Thus, minimizing the usage of Pd is necessary.

In order to investigate the electronic state changes, we performed ex situ X-ray photoemission spectroscopy (XPS) (Figure S12) and operando Raman spectroscopy (Figure S13). The ex situ XPS analysis indicates that Cu gets oxidized after the reaction (Figure S12). In order to verify that, operando Raman spectroscopy (Methods, Figure S13) was performed under the given potentials. Cu species showed no signal in Raman spectroscopy. With the increase of the applied voltage, the characteristic peaks of CuO, Cu_2O, and PdO gradually appeared (Figure S13). The following characteristic peaks were observed for the PdCu SAA samples: (1) CuO at 298 and 629 cm^{-1}, (2) Cu_2O stretching at 436 cm^{-1}, and (3) PdO at 725 and 929 cm^{-1}.[28−33] This indicates that both the oxidation states of Cu and Pd increased during the reaction. This may be due to the production of the OH* radical from H_2O.[34]

We also measured the electrochemical surface area (ECSA) of Cu and PdCu SAA based on the electrochemical double-layer capacitance. As presented (Figure S14), the estimated ECSAs of Cu and PdCu SAA are 1.7 and 11.7 cm^{-2}, respectively. The yields based on the ECSA of Cu are much larger than those of PdCu SAA under various potentials. It is reasonable to suppose that the increase of the ECSA improves the yield. The focus of this work is the selectivity, and the promoting effect of the ECSA on the yield does not affect the conclusion that the PdCu SAA active site structure benefits the high selectivity of the NH_3 product.

Single-Crystal Electrocatalytic Performance and DFT Calculations. The material characterization and electrochemical results above demonstrate the advantages of PdCu SAA with Pd single atoms in improving the NO_3^-RR performance. To explore the active sites of the reaction and whether it has a facet-dependent behavior, single-crystal experiments were carried out. The GIXRD spectrum of PdCu SAA (Figure 2A) shows its polycrystalline nature, including Cu (100), (110), and (111) Bragg reflections. To confirm the most active facet with the Pd single atom, the Pd single atom was doped on single-crystal Cu with different crystal facets, namely, Cu (100), Cu (110), and Cu (111). XRD results show that the Pd doping does not produce a new crystal peak, indicating that no Pd crystals were formed (Figure 4A and Figure S15A). EXAFS results further demonstrate the single-atom dispersion of Pd atoms in the single-crystal Cu (Figure 4B and Figure S15B−I). The white line of all PdCu single-crystal samples shows a shift to lower energy for the adsorption edge (E_0) compared to that of Pd foil (Figure

https://doi.org/10.1021/acscatal.3c01088
ACS Catal. 2023, 13, 10560−10569

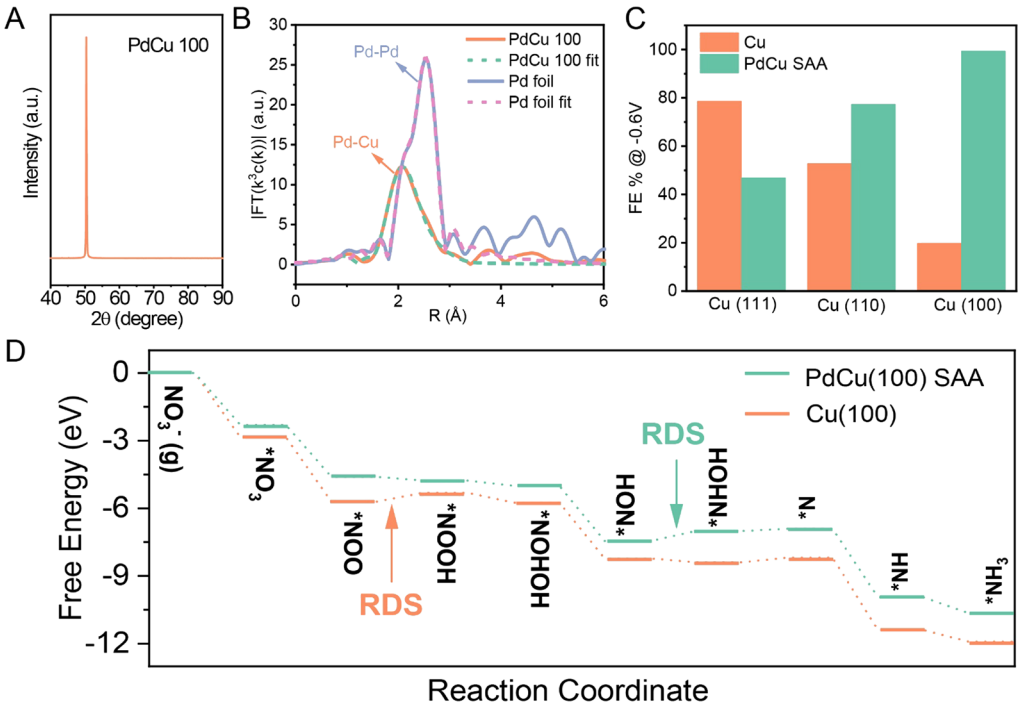

Figure 4. Single-crystal electrocatalytic performance and DFT calculations. (A) GIXRD spectra of PdCu SAA based on single-crystal Cu 100. (B) Pd K-edge Fourier-transform EXAFS spectra of single-crystal-based PdCu SAA based on single-crystal Cu 100 and Pd foil reference. (C) NH_3 FE results of single-crystal Cu and relative PdCu SAA. (D) Gibbs free energy diagram and reaction pathway of various intermediates generated during electrocatalytic NO_3^-RR over Cu (100) and PdCu(100) SAA.

S15B,C), suggesting electron transfer from Cu to Pd due to the formation of the Pd−Cu bond, which agrees well with the results of Bader charge analysis in Figure 2C. It is worth noting that the smallest shift of PdCu (100) shifts among all PdCu single-crystal samples means the lowest negative charge of Pd in PdCu (100) (Figure S15C), indicating that the Pd atoms on the Cu(100) surface will not strongly adsorb *H and hinder the following hydrogenation step on neighboring Cu sites. The detailed fitting results are shown in Table S3. The PdCu (100) SAA single crystal exhibits the highest NH_3 production FE of 99%, which is much higher than that of PdCu (110) SAA and PdCu (111) SAA (Figure 4C and Figure S16A,B). Those results indicate that Cu (100) should be the most active crystal facet for Pd single-atom support for the NO_3^-RR reaction. Then, DFT calculations were conducted to investigate the reaction mechanism based on the PdCu (100) model (Figure S17). In the reaction pathway (Figure 4D), NO_3^- was adsorbed on the single-atom Pd site and formed $*NO_3$ with an energy decrease. The N−O bond in $*NO_3$ was then cleaved to produce *NOO. Next, two H atoms bound with O to form *NOOH and *NOHOH successively. With two further hydrogenation steps, *NOHOH was transformed into *NHOH. After losing one H_2O molecule, the active *N was formed. Subsequently, $*NH_3$ was formed through a series of hydrogenation steps from *N and then finally desorbed from the catalyst. Notably, the RDS for Cu (100) is the hydrogenation of *NOO with an energy barrier of 0.39 eV while the RDS for PdCu (100) is the formation of *NHOH with an energy barrier of only 0.10 eV. As a result, the reaction was facilitated over PdCu (100), which is consistent with the experimental observation.

CONCLUSIONS

In conclusion, a novel PdCu SAA was fabricated based on a facile galvanic replacement reaction and exhibited an ultrahigh FE of 97.1% with a yield of 15.4 μmol cm^{-2} h^{-1} toward NH_3 production in the NO_3^-RR under mild neutral media. Single-crystal experiments and DFT calculations reveal that the atomic Pd sites on Cu (100) facets are the most likely active sites. The Pd sites exhibit a facet-dependent behavior. Typically, with the introduction of single-atom Pd, the RDS on Cu changed from *NOO → *NOOH with an energy barrier of 0.39 eV to *NOH → *NHOH with an energy barrier of 0.10 eV on PdCu SAA. This work not only develops an effective catalyst for NH_3 production from nitrate reduction in mild neutral media but also demonstrates the promising application of SAAs in NO_3^-RR for nitrate nutrition recovery from wastewater and other selective electrocatalytic applications.

METHODS

Chemicals. Toray HCP-060 CP was purchased from Fuel Cell Store. D_2O, $^{15}NH_4Cl$, $Na^{15}NO_3$, NH_4Cl, $NaNO_3$, NaOH, Na_2PdCl_4, Cu $(NO_3)_2*3H_2O$, sodium citrate dehydrates, salicylic acid, acetone, ethanol, ethylene glycol, isopropanol, NaClO aqueous solution, sodium nitroprusside ($C_5FeN_6Na_2O$), and *p*-dimethylaminobenzaldehyde were purchased from Sigma. Cu single crystals with different crystal facets were purchased from MTI company. Deionized water was used in the experiments. All reagents were used without further purification.

Electrodeposition of Cu. Before the electrodeposition process, CP was first cut into a 1 cm × 2 cm size and then fully washed with acetone, dilute HCl solution, and water. Electrodeposition was conducted using a three-electrode

https://doi.org/10.1021/acscatal.3c01088
ACS Catal. 2023, 13, 10560−10569

system, in which CP served as the working electrode with a 1 × 1 cm^2 working area. The reference electrode and counter electrode were an Ag/AgCl electrode and a graphite rod, respectively. The electrochemical technique used for electrodeposition was the potentiostat method. The potentiostat electrodeposition was conducted in 50 mL of 6.5 mM $Cu(NO_3)_2$ aqueous solution with CP as the substrate under the potential of −0.3 V (vs Ag/AgCl) for 30 min.[35] Under the application of the electric field, Cu^{2+} was reduced into Cu nanoparticles on the CP. Meanwhile, H_2O was oxidized into O_2 at the graphite rod. After the electrodeposition, the CP with Cu nanoparticles was washed with isopropanol and water. After being dried by N_2 flow, the Cu sample was stored in a vacuum or inert gas environment.

Synthesis of PdCu SAA. PdCu SAA was synthesized by the galvanic replacement reaction. The galvanic replacement reaction was spontaneously driven by their reduction potential difference. Typically, 2 mL of 0.1 mg mL^{-1} Na_2PdCl_4 solution was first prepared using ethylene glycol as solvent. Then, CP with Cu nanoparticles was immersed into the solution under 80 °C for 15 min. After washing with isopropanol and water, the CP with PdCu SAA was dried by N_2 flow and was stored in a vacuum or inert gas environment for further experiments. For the synthesis of PdCu alloy NP and Pd NP on Cu, the concentrations of Na_2PdCl_4 solution were increased to 5 and 100 mg mL^{-1}, respectively. The other procedures were the same as that for PdCu SAA on CP. Single-crystal PdCu SAA was synthesized according to a similar procedure, which put single-crystal Cu into a dilute Na_2PdCl_4 solution (0.001 mg mL^{-1}) for 15 min at room temperature. The other procedures were the same as that for PdCu SAA on CP. The CP is to enhance the conductivity of the electrode during the electrocatalytic reaction.

Material Characterization. SEM images were captured on a Hitachi S-4800 with a working accelerating voltage of 10 kV. Glancing-incidence X-ray diffraction (GIXRD) was measured on a PANalytical X'Pert Pro MRD diffractometer with Cu Kα radiation (1.54 Å) at an incidence angle of 0.3°. XPS measurements were carried out on a Thermo-VG Scientific ESCALAB 250 microprobe with a monochromatic Al Kα X-ray source (1486.6 eV). The obtained spectra were calibrated using the C 1s line. The catalyst was sonicated from the CP in IPA solution. Then, the solvent was drop-cast onto ultrathin lacey carbon TEM grids for imaging. Some residue CP is hard to separate from the samples. Aberration-corrected high-angle annular dark-field scanning transmission electron microscopy (AC-HAADF-STEM) tests were carried out on an FEI Titan 80-300 HB TEM equipped with an EDX at 300 kV. The HAADF-STEM images were recorded by the FEI Titan 80-300 HB TEM/STEM with double aberration correctors operating at 300 kV at the Canadian Center for Electron Microscopy (CCEM). Inductively coupled plasma mass spectrometry (ICP-MS) analyses were carried out on an Agilent 8800 triple quadrupole instrument, using He as a collision cell gas, Ge and In as internal standards to correct for instrument drift, and ICP element standards (secondary standards from Delta Scientific Inorganic Ventures; primary calibration standards from Alfa Aesar and ARISTAR VWR Chemicals BDH) to confirm instrument accuracy (within 5%; the relative standard deviation for individual sample analyses was ≤11%). UV−vis absorption spectroscopy was tested on a Shimadzu UV-2600i spectrophotometer. Proton nuclear magnetic resonance (H-NMR) was measured on Bruker Avance III 300 MHz. XAS measurements were carried out at the 20-BM and 20-ID-C beamline of the Advanced Photon Source (APS), Argonne National Laboratory. The measurements at the Pd K-edge were performed in fluorescence mode using a Lytle detector. The Pd K-edge XANES and EXAFS data were analyzed and treated using the software package Athena. The EXAFS data was fitted using the software package Artemis. Pd foil was applied for reference and calibration samples. In this fitting data, CN represents the coordination numbers of identical atoms; R is assigned as the interatomic distance; δ^2 is considered as Debye−Waller factors. The fitting parameters strictly comply with all experimental requirements.

Electrochemical NO_3^-RR Measurements. All electrochemical tests were measured on Autolab PGSTAT204 electrochemical workstations at room temperature with IR correction. A three-electrode system was fabricated with the prepared PdCu-based materials, platinum wire, and saturated calomel electrode (SCE) serving as the working electrode, the counter electrode, and the reference electrode, respectively. A gas-tight H-type electrochemical cell equipped with a piece of 211 Nafion membrane was employed to conduct the electrochemical reaction. A platinum wire was in the anode compartment alone to avoid the electrochemical oxidation of produced NH_3. Before NO_3^-RR tests, the 211 Nafion membrane was first activated in 5% H_2O_2, H_2O, 0.5 M H_2SO_4, and H_2O for 20 min and then soaked in water at 80 °C for 12 h.[36] The synthesized CP with the PdCu SAA catalyst directly served as the working electrode with an electrode holder. The NO_3^-RR catalytic activities were evaluated using the potentiostatic technique under selective potential for 1 h in 0.5 M Na_2SO_4 with 600 ppm $NaNO_3$ solution under an Ar gas environment. All the potential values are presented in RHE unless otherwise stated. For the electrochemical test of single-crystal PdCu SAA samples, the bulk single-crystal PdCu SAA was connected to the electrode holder through Cu foil. To avoid the interference of Cu foil on the electrochemical signal, an inert Kapton tap was used to totally cover the Cu foil.

Determination of Ammonia Using the UV−vis Method. The UV−vis method for NH_3 concentration determination was modified from the indophenol blue method.[37] In detail, 2 mL of the electrolyte was taken out after the electrocatalytic reaction and diluted five times. Then, 2 mL of the diluted solution was added to 2 mL of a 1 M NaOH solution containing salicylic acid and sodium citrate. Then, 1 mL of 0.05 M NaClO and 0.2 mL of 1 wt % $C_5FeN_6Na_2O$ were also added to the above-mixed solution. The UV−vis absorption spectrum was measured after 2 h. The concentration of indophenol blue was determined using the absorbance at the wavelength of 655 nm. The concentration−absorbance curves were calibrated using a standard ammonia nitrate solution with a series of concentrations in 0.5 M Na_2SO_4. The fitting curve ($y = 0.160x + 0.040$, $R^2 = 0.999$) shows a good linear relationship between the absorbance values and NH_3 concentrations (Figure S7A,B).

Determination of Ammonia Using the NMR Method. The NMR method is based on H-NMR. To better detect the NH_4^+ using NMR, the solution needs to be acidized to pH ∼ 3. Typically, 630 μL of electrolyte was taken out after the electrocatalytic reaction and then acidized by adding 5 μL of concentrated hydrochloric acid. After that, 100 μL of D_2O with certain DMSO was added to the mixed solution and then transferred into an NMR tube for the test. All NMR spectra were obtained by 128 scans. DMSO shows a peak at 2.6 ppm

https://doi.org/10.1021/acscatal.3c01088
ACS Catal. 2023, 13, 10560−10569

and serves as the internal standard. The concentration of NH_4^+ was determined by the peak (triplet) area ratio between NH_4^+ and DMSO. The concentration−NMR peak area ratio curves were calibrated using a standard NH_4Cl solution with a series of concentrations in 0.5 M Na_2SO_4. The fitting curve ($y = 0.007x - 0.005$, $R^2 = 0.999$) shows a good linear relationship between the absorbance values and NH_3 concentrations (Figure S7C,D).

Isotope Labeling Experiments. The isotopic labeling experiments were conducted using $^{15}NaNO_3$ as the feeding in 0.5 M Na_2SO_4. All other experimental operations are the same as that using $NaNO_3$. Especially, the $^{15}NH_4^+$ standard curve was built using $^{15}NH_4Cl$ with a series of concentrations in 0.5 M Na_2SO_4. The fitting curve ($y = 0.010x - 0.009$, $R^2 = 0.999$) shows a good linear relationship between the absorbance values and NH_3 concentrations (Figure S7E,F).

Calculations of the NH_3 Formation Rate and FE. The FE and yield for NH_3 are calculated as follows:

$$\text{yield} = \frac{c_{NH3} \times V \times M_{NH3}}{A \times t}$$

$$\text{FE} = \frac{c_{NH3} \times V \times 8 \times F}{\int_0^t i dt}$$

where c_{NH3} is the determined NH_3 concentration; V is the volume of electrolyte in the cathode compartment, typically 25 mL; M_{NH3} is the molecular weight of ammonia, 17 g mol^{-1} for $^{14}NH_3$ and 18 g mol^{-1} for $^{15}NH_3$; A is the geometric surface area of the electrode, 1 cm^2; t is the time of electrolysis, 3600 s; and F is the Faraday constant, i.e., 96,485 C mol^{-1}. The reported values of yield and FE were calculated based on three separate measurements under the same conditions.

Operando Raman Spectroscopy. The operando Raman spectroscopy measurements were performed using a Renishaw inVia Reflex system and an Autolab PGSTAT204 electrochemical workstation. The electrochemical cell was homemade by Teflon with a quartz window between the sample and objective. The working electrode was immersed into the electrolyte through the wall of the cell, and the electrode plane was kept perpendicular to the laser. A platinum wire and Ag/AgCl electrode were served as the counter and reference electrodes, respectively. IT curves were conducted at 0, −1.1, −1.2, and −1.3 V vs. Ag/AgCl.

ECSA Measurement. Cyclic voltammetry (CV) curves in electrochemical double-layer capacitance (C_{dl}) determination were measured in a potential window nearly without the Faradaic process at different scan rates of 20, 40, 60, 80, and 100 mV s^{-1}. The plot of current density at the set potential against scan rate has a linear relationship, and its slope is the C_{dl}. What should be noted is that the double-layer capacitance for the ideal smooth oxide surface is assumed to be 60 $\mu F \cdot cm^{-2}$ based on previous reports,[38−40] which means that the ECSA values can only be used for reference and related comparison.

Determination of NO_2^- Using the UV−vis-Absorption Method. The method of NO_2^- using the UV−vis-absorption method is similar from a previous report.[15] A mixture of *p*-aminobenzenesulfonamide (4 g), *N*-(1-naphthyl) ethylenediamine dihydrochloride (0.2 g), ultrapure water (50 mL), and phosphoric acid (10 mL, ρ = 1.70 g/mL) was used as a color reagent. A certain amount of electrolyte was taken out from the electrolytic cell and diluted to 5 mL to the detection range. Next, 0.1 mL of color reagent was added into the aforementioned 5 mL solution and mixed uniformity, and the absorption intensity at a wavelength of 540 nm was recorded after sitting for 20 min. The concentration−absorbance curves were calibrated using a standard ammonia nitrate solution with a series of concentrations in 0.5 M Na_2SO_4. The fitting curve ($y = 0.6193x + 0.0022$, $R^2 = 0.9999$) shows a good linear relationship between the absorbance values and NO_2^- concentrations (Figure S9A,B). The FE of NO_2^- was then calculated.

DFT Calculations. DFT calculations were performed using the Vienna Ab initio Simulation Package (VASP) with projector-augmented wave pseudopotentials.[41−43] The Perdew-Burke-Ernzerhof (PBE) exchange-correlation functional within the generalized gradient approximation (GGA) was chosen in consideration of a balance between accuracy and computational cost.[44] van der Waals interactions were considered using DFT-D3 with the Becke−Johnson damping method. The plane wave energy cutoff was 400 eV for each of the slabs. These periodic slabs were separated by 20 Å vacuum space along the *z*-direction to isolate interactions between replicas. The Brillouin zone was sampled on a 3 × 2 × 1 Monkhorst−Pack *k*-point grid.[45] For each slab, the top two layers of the slabs and adsorbates were fully relaxed until the maximum forces converged to 0.05 eV/Å. Free energy for the three catalysts was obtained following the same method as the literature.[46] The free energy correction was implemented for each species by conducting an additional frequency calculation with the same function. To avoid abnormal entropy contribution, frequencies less than 50 cm^{-1} are set to 50 cm^{-1}.

■ ASSOCIATED CONTENT

Data Availability Statement

The authors declare that all data supporting this study are available within the paper and Supplementary Information files. Source data are provided in this paper.

Supporting Information

The Supporting Information is available free of charge at https://pubs.acs.org/doi/10.1021/acscatal.3c01088.

SEM images for blank carbon paper and all catalyst samples; AC-HAADF-STEM images of the catalysts; SEM-EDX maps; EXAFS fitting results of Pd L-edge in PdCu SAA and Pd foil; LSV measurement; electrochemical, UV, and NMR data of the NO_3^- reduction data of Cu and PdCu SAA catalysts; standard curves of NH_3 from different detection methods; *i*−*t* curves and NH_3 FE results of 10 h stability test of the PdCu SAA catalyst; measurement of NO_2^- products; GIXRD patterns for increasing the Pd loading amount; effect of increasing amount of Pd loading on Cu; ex situ XPS analysis; operando Raman spectroscopy during the electrocatalytic NO_3^- reduction reaction; ECSA and yield measurement; characterization of PdCu SAA based on Cu single crystals; electrochemical and UV data of the single-crystal samples; DFT model of PdCu (100); fitted EXAFS parameters at the Pd K-edge for PdCu SAA based on Cu nanoparticles and Pd foil; comparison with recently reported catalysts under neutral media; fitted EXAFS parameters at the Pd K-edge for PdCu SAA based on Cu single crystals (PDF)

https://doi.org/10.1021/acscatal.3c01088
ACS Catal. 2023, 13, 10560−10569

AUTHOR INFORMATION

Corresponding Author

Yimin A. Wu − *Department of Mechanical and Mechatronics Engineering, Materials Interfaces Foundry, Waterloo Institute for Nanotechnology, Department of Chemistry, Water Institute, and Waterloo Climate Institute, University of Waterloo, Waterloo, Ontario N2L 3G1, Canada;* orcid.org/0000-0002-3807-8431; Email: yimin.wu@uwaterloo.ca

Authors

Cheng Du − *Department of Mechanical and Mechatronics Engineering, Materials Interfaces Foundry, Waterloo Institute for Nanotechnology, University of Waterloo, Waterloo, Ontario N2L 3G1, Canada*

Siyan Lu − *Department of Mechanical and Mechatronics Engineering, Materials Interfaces Foundry, Waterloo Institute for Nanotechnology, University of Waterloo, Waterloo, Ontario N2L 3G1, Canada*

Jia-ao Wang − *Department of Chemistry and the Oden Institute for Computational Engineering and Sciences, The University of Texas at Austin, Austin, Texas 78712-0165, United States;* orcid.org/0000-0002-4944-4951

Xiyang Wang − *Department of Mechanical and Mechatronics Engineering, Materials Interfaces Foundry, Waterloo Institute for Nanotechnology, University of Waterloo, Waterloo, Ontario N2L 3G1, Canada;* orcid.org/0000-0002-7591-6676

Maoyu Wang − *X-Ray Science Division, Argonne National Laboratory, Lemont, Illinois 60439, United States*

Holly M. Fruehwald − *Department of Chemistry, University of Waterloo, Waterloo, Ontario N2L 3G1, Canada*

Lei Wang − *Department of Mechanical and Mechatronics Engineering, Materials Interfaces Foundry, Waterloo Institute for Nanotechnology, University of Waterloo, Waterloo, Ontario N2L 3G1, Canada*

Baizhou Zhang − *Department of Mechanical and Mechatronics Engineering, Materials Interfaces Foundry, Waterloo Institute for Nanotechnology, University of Waterloo, Waterloo, Ontario N2L 3G1, Canada*

Tao Guo − *Department of Mechanical and Mechatronics Engineering, Materials Interfaces Foundry, Waterloo Institute for Nanotechnology, University of Waterloo, Waterloo, Ontario N2L 3G1, Canada*

Joel P. Mills − *Department of Mechanical and Mechatronics Engineering, Materials Interfaces Foundry, Waterloo Institute for Nanotechnology, University of Waterloo, Waterloo, Ontario N2L 3G1, Canada*

Wei Wei − *Department of Mechanical and Mechatronics Engineering, Materials Interfaces Foundry, Waterloo Institute for Nanotechnology, University of Waterloo, Waterloo, Ontario N2L 3G1, Canada*

Zuolong Chen − *Department of Mechanical and Mechatronics Engineering, Materials Interfaces Foundry, Waterloo Institute for Nanotechnology, University of Waterloo, Waterloo, Ontario N2L 3G1, Canada*

Youchao Teng − *Department of Mechanical and Mechatronics Engineering, Materials Interfaces Foundry, Waterloo Institute for Nanotechnology, University of Waterloo, Waterloo, Ontario N2L 3G1, Canada*

Jingyan Zhang − *Department of Mechanical and Mechatronics Engineering, Materials Interfaces Foundry, Waterloo Institute for Nanotechnology, University of Waterloo, Waterloo, Ontario N2L 3G1, Canada*

Cheng-Jun Sun − *X-Ray Science Division, Argonne National Laboratory, Lemont, Illinois 60439, United States*

Hua Zhou − *X-Ray Science Division, Argonne National Laboratory, Lemont, Illinois 60439, United States;* orcid.org/0000-0001-9642-8674

Rodney D. L. Smith − *Department of Chemistry, University of Waterloo, Waterloo, Ontario N2L 3G1, Canada;* orcid.org/0000-0003-1209-9653

Brian Kendall − *Department of Earth and Environmental Sciences, University of Waterloo, Waterloo, Ontario N2L 3G1, Canada*

Graeme Henkelman − *Department of Chemistry and the Oden Institute for Computational Engineering and Sciences, The University of Texas at Austin, Austin, Texas 78712-0165, United States;* orcid.org/0000-0002-0336-7153

Complete contact information is available at: https://pubs.acs.org/10.1021/acscatal.3c01088

Author Contributions

#C.D., S.L., and J.-a.W. equally contributed to this study.

Author Contributions

Y.A.W. conceived and supervised the research. C.D. and S.L. carried out the catalyst synthesis, characterization, and performance test. J.-a.W. and G.H. performed the DFT calculations. M.W., H.Z., and C.-J.S carried out the XAFS measurements. X.W. performed the XAFS data fitting. S.L., L.W., H.M.F., and R.D.L.S. measured the operando Raman spectroscopy. B.Z., T.G., J.P.M., W.W., L.W., Z.C., Y.T., and J.Z. assisted in the material synthesis, characterizations, and performance test. B.K. performed all ICP-MS tests. C.D., S.L., and Y.A.W. wrote the manuscript. All authors commented on the manuscript.

Notes

The authors declare the following competing financial interest(s): Y.A.W., C.D., and S.L. have filed a US patent application through the University of Waterloo on this technology related to this CuPd single-atom alloy for nutrition recovery from waste water (US Patent application number 63/475,329). The remaining authors declare no competing interests.

All the DFT calculations were performed using the commercial software VASP. All the input and output files of the calculations are available on request.

Supplementary information is available for this paper. Correspondence and requests for materials should be addressed to Y.A.W.

ACKNOWLEDGMENTS

Y.A.W. thanks the funding from Tang Family Chair in New Energy Materials and Sustainability, the Natural Sciences and Engineering Research Council of Canada (NSERC) (RGPIN-2020-05903, GECR-2020-00476), the seed funding from the Water Institute (WI), and Waterloo Climate Institute (WCI) at the University of Waterloo. Transmission electron microscopy was performed at the Canadian Centre for Electron Microscopy (also supported by NSERC and other government agencies). This research used resources from the Advanced Photon Source, an Office of Science User Facility operated for the U.S. Department of Energy (DOE) Office of Science by Argonne National Laboratory, and was supported

by the U.S. DOE under Contract No. DE-AC02-06CH11357 and the Canadian Light Source and its funding partners. The calculations were supported by the Welch Foundation (F-1841) and the Texas Advanced Computing Center. We acknowledge the discussion with Bryce Kieffer.

REFERENCES

(1) Van Langevelde, P. H.; Katsounaros, I.; Koper, M. T. M. Electrocatalytic Nitrate Reduction for Sustainable Ammonia Production. *Joule* **2021**, *5*, 290−294.
(2) Wang, Y. T.; Wang, C. H.; Li, M. Y.; Yu, Y. F.; Zhang, B. Nitrate electroreduction: mechanism insight, in situ characterization, performance evaluation, and challenges. *Chem. Soc. Rev.* **2021**, *50*, 6720−6733.
(3) Zeng, Y. C.; Priest, C.; Wang, G. F.; Wu, G. Restoring the Nitrogen Cycle by Electrochemical Reduction of Nitrate: Progress and Prospects. *Small Methods* **2020**, *4*, 2000672.
(4) Xu, H.; Wu, J.; Luo, W.; Li, Q.; Zhang, W. X.; Yang, J. P. Dendritic Cell-Inspired Designed Architectures toward Highly Efficient Electrocatalysts for Nitrate Reduction Reaction. *Small* **2020**, *16*, 2001775.
(5) Rosca, V.; Duca, M.; de Groot, M. T.; Koper, M. T. M. Nitrogen Cycle Electrocatalysis. *Chem. Rev.* **2009**, *109*, 2209−2244.
(6) Andersen, S. Z.; Colic, V.; Yang, S.; Schwalbe, J. A.; Nielander, A. C.; McEnaney, J. M.; Enemark-Rasmussen, K.; Baker, J. G.; Singh, A. R.; Rohr, B. A.; Statt, M. J.; Blair, S. J.; Mezzavilla, S.; Kibsgaard, J.; Vesborg, P. C. K.; Cargnello, M.; Bent, S. F.; Jaramillo, T. F.; Stephens, I. E. L.; Norskov, J. K.; Chorkendorff, I. A rigorous electrochemical ammonia synthesis protocol with quantitative isotope measurements. *Nature* **2019**, *570*, 504−508.
(7) Fang, C.; Lu, B.; Pawar, G.; Zhang, M.; Cheng, D.; Chen, S.; Ceja, M.; Doux, J.-M.; Musrock, H.; Cai, M.; Liaw, B.; Meng, Y. S. Pressure-tailored lithium deposition and dissolution in lithium metal batteries. *Nat. Energy* **2021**, *6*, 987−994.
(8) Du, C.; Qiu, C.; Fang, Z.; Li, P.; Gao, Y.; Wang, J.; Chen, W. Interface hydrophobic tunnel engineering: A general strategy to boost electrochemical conversion of N_2 to NH_3. *Nano Energy* **2022**, *92*, No. 106784.
(9) Xu, H.; Ma, Y.; Chen, J.; Zhang, W.-x.; Yang, J. Electrocatalytic reduction of nitrate − a step towards a sustainable nitrogen cycle. *Chem. Soc. Rev.* **2022**, *51*, 2710−2758.
(10) Hu, Q.; Qin, Y.; Wang, X.; Wang, Z.; Huang, X.; Zheng, H.; Gao, K.; Yang, H.; Zhang, P.; Shao, M.; He, C. Reaction intermediate-mediated electrocatalyst synthesis favors specified facet and defect exposure for efficient nitrate−ammonia conversion. *Energy Environ. Sci.* **2021**, *14*, 4989−4997.
(11) Ye, S.; Chen, Z.; Zhang, G.; Chen, W.; Peng, C.; Yang, X.; Zheng, L.; Li, Y.; Ren, X.; Cao, H.; Xue, D.; Qiu, J.; Zhang, Q.; Liu, J. Elucidating the activity, mechanism and application of selective electrosynthesis of ammonia from nitrate on cobalt phosphide. *Energy Environ. Sci.* **2022**, *15*, 760−770.
(12) Liu, H.; Lang, X.; Zhu, C.; Timoshenko, J.; Rüscher, M.; Bai, L.; Guijarro, N.; Yin, H.; Peng, Y.; Li, J.; Liu, Z.; Wang, W.; Cuenya, B. R.; Luo, J. Efficient Electrochemical Nitrate Reduction to Ammonia with Copper-Supported Rhodium Cluster and Single-Atom Catalysts. *Angew. Chem., Int. Ed.* **2022**, *61*, No. e202202556.
(13) Duca, M.; Koper, M. T. M. Powering denitrification: the perspectives of electrocatalytic nitrate reduction. *Energy Environ. Sci.* **2012**, *5*, 9726−9742.
(14) Zhu, T.; Chen, Q.; Liao, P.; Duan, W.; Liang, S.; Yan, Z.; Feng, C. Single-Atom Cu Catalysts for Enhanced Electrocatalytic Nitrate Reduction with Significant Alleviation of Nitrite Production. *Small* **2020**, *16*, 2004526.
(15) Wang, Y.; Zhou, W.; Jia, R.; Yu, Y.; Zhang, B. Unveiling the Activity Origin of a Copper-based Electrocatalyst for Selective Nitrate Reduction to Ammonia. *Angew. Chem., Int. Ed.* **2020**, *59*, 5350−5354.
(16) Chen, G.-F.; Yuan, Y.; Jiang, H.; Ren, S.-Y.; Ding, L.-X.; Ma, L.; Wu, T.; Lu, J.; Wang, H. Electrochemical reduction of nitrate to ammonia via direct eight-electron transfer using a copper−molecular solid catalyst. *Nat. Energy* **2020**, *5*, 605−613.
(17) Wang, Y.; Xu, A.; Wang, Z.; Huang, L.; Li, J.; Li, F.; Wicks, J.; Luo, M.; Nam, D. H.; Tan, C. S.; Ding, Y.; Wu, J.; Lum, Y.; Dinh, C. T.; Sinton, D.; Zheng, G.; Sargent, E. Enhanced Nitrate-to-Ammonia Activity on Copper-Nickel Alloys via Tuning of Intermediate Adsorption. *J. Am. Chem. Soc.* **2020**, *142*, 5702−5708.
(18) Xu, Y.; Ren, K.; Ren, T.; Wang, M.; Liu, M.; Wang, Z.; Li, X.; Wang, L.; Wang, H. Cooperativity of Cu and Pd active sites in CuPd aerogels enhances nitrate electroreduction to ammonia. *Chem. Commun.* **2021**, *57*, 7525−7528.
(19) Simpson, B. K.; Johnson, D. C. Electrocatalysis of nitrate reduction at copper-nickel alloy electrodes in acidic media. *Electroanalysis* **2004**, *16*, 532−538.
(20) Mattarozzi, L.; Cattarin, S.; Comisso, N.; Guerriero, P.; Musiani, M.; Vazquez-Gomez, L.; Verlato, E. Electrochemical reduction of nitrate and nitrite in alkaline media at CuNi alloy electrodes. *Electrochim. Acta* **2013**, *89*, 488−496.
(21) Sarkar, S.; Peter, S. C. An overview on Pd-based electrocatalysts for the hydrogen evolution reaction. *Inorg. Chem. Front.* **2018**, *5*, 2060−2080.
(22) Du, C.; He, S.; Liu, M.; Gao, X.; Zhang, R.; Chen, W. Novel $Pd_{13}Cu_3S_7$ nanotubes with high electrocatalytic activity towards both oxygen reduction and ethanol oxidation reactions. *CrystEngComm* **2016**, *18*, 6055−6061.
(23) Xia, X.; Wang, Y.; Ruditskiy, A.; Xia, Y. 25th Anniversary Article: Galvanic Replacement: A Simple and Versatile Route to Hollow Nanostructures with Tunable and Well-Controlled Properties. *Adv. Mater.* **2013**, *25*, 6313−6333.
(24) Lugg, N. R.; Kumamoto, A.; Ishikawa, R.; Feng, B.; Kothleitner, G.; Shibata, N.; Ikuhara, Y. Atomic-Resolution Composition Mapping in EDS STEM. *Microsc. Microanal.* **2016**, *22*, 1432.
(25) Spurgeon, S. R.; Du, Y.; Chambers, S. A. Measurement error in atomic-scale scanning transmission electron microscopy—energy-dispersive X-ray spectroscopy (STEM-EDS) mapping of a model oxide interface. *Microsc. Microanal.* **2017**, *23*, 513−517.
(26) Pei, G.; Liu, X.; Chai, M.; Wang, A.; Zhang, T. Isolation of Pd atoms by Cu for semi-hydrogenation of acetylene: Effects of Cu loading. *Chin. J. Catal.* **2017**, *38*, 1540−1548.
(27) Jiang, L.; Liu, K.; Hung, S.; Zhou, L.; Qin, R.; Zhang, Q.; Liu, P.; Gu, L.; Chen, H.; Fu, G.; Zheng, N. Facet engineering accelerates spillover hydrogenation on highly diluted metal nanocatalysts. *Nat. Nanotechnol.* **2020**, *15*, 848−853.
(28) Mao, Y.; He, J.; Sun, X.; Li, W.; Lu, X.; Gan, J.; Liu, Z.; Gong, L.; Chen, J.; Liu, P.; Tong, Y. Electrochemical synthesis of hierarchical Cu2O stars with enhanced photoelectrochemical properties. *Electrochim. Acta* **2012**, *62*, 1−7.
(29) Tran, T. H.; Nguyen, V. T. Phase transition of Cu_2O to CuO nanocrystals by selective laser heating. *Mater. Sci. Semicond. Process.* **2016**, *46*, 6−9.
(30) Hsu, Y.-K.; Yu, C.-H.; Chen, Y.-C.; Lin, Y.-G. Fabrication of coral-like Cu_2O nanoelectrode for solar hydrogen generation. *J. Power Sources* **2013**, *242*, 541−547.
(31) Solache-Carranco, H.; Juarez-Diaz, G.; Galvan-Arellano, M.; Martinez-Juarez, J.; Pena-Sierra, R. In *Raman scattering and photoluminescence studies on Cu 2 O, 2008 5th International Conference on Electrical Engineering, Computing Science and Automatic Control*, IEEE: 2008; pp. 421−424.
(32) Kumari, T.; Gopal, R.; Goyal, A.; Joshi, J. Sol−gel synthesis of Pd@ PdO core−shell nanoparticles and effect of precursor chemistry on their structural and optical properties. *J. Inorg. Organomet. Polym. Mater.* **2019**, *29*, 316−325.
(33) Baylet, A.; Marecot, P.; Duprez, D.; Castellazzi, P.; Groppi, G.; Forzatti, P. In situ Raman and in situ XRD analysis of PdO reduction and Pd° oxidation supported on γ-Al_2O_3 catalyst under different atmospheres. *Phys. Chem. Chem. Phys.* **2011**, *13*, 4607−4613.
(34) Mu, S.; Lu, H.; Wu, Q.; Li, L.; Zhao, R.; Long, C.; Cui, C. Hydroxyl radicals dominate reoxidation of oxide-derived Cu in electrochemical CO2 reduction. *Nat. Commun.* **2022**, *13*, 3694.

https://doi.org/10.1021/acscatal.3c01088
ACS Catal. 2023, 13, 10560−10569

(35) Chen, Z.; Wang, T.; Liu, B.; Cheng, D.; Hu, C.; Zhang, G.; Zhu, W.; Wang, H.; Zhao, Z.-J.; Gong, J. Grain-Boundary-Rich Copper for Efficient Solar-Driven Electrochemical CO_2 Reduction to Ethylene and Ethanol. *J. Am. Chem. Soc.* **2020**, *142*, 6878−6883.
(36) Hanifpour, F.; Sveinbjornsson, A.; Canales, C. P.; Skulason, E.; Flosadottir, H. D. Preparation of Nafion Membranes for Reproducible Ammonia Quantification in Nitrogen Reduction Reaction Experiments. *Angew. Chem., Int. Ed.* **2020**, *59*, 22938−22942.
(37) Zhu, D.; Zhang, L. H.; Ruther, R. E.; Hamers, R. J. Photo-illuminated diamond as a solid-state source of solvated electrons in water for nitrogen reduction. *Nat. Mater.* **2013**, *12*, 836−841.
(38) Chi, B.; Lin, H.; Li, J. Cations distribution of $CuxCo_{3-x}O_4$ and its electrocatalytic activities for oxygen evolution reaction. *Int. J. Hydrogen Energy* **2008**, *33*, 4763−4768.
(39) Chi, B.; Lin, H.; Li, J.; Wang, N.; Yang, J. Comparison of three preparation methods of $NiCo_2O_4$ electrodes. *Int. J. Hydrogen Energy* **2006**, *31*, 1210−1214.
(40) Tiwari, S.; Samuel, S.; Singh, R.; Poillerat, G.; Koenig, J.; Chartier, P. Active thin NiCo2O4 film prepared on nickel by spray pyrolysis for oxygen evolution. *Int. J. Hydrogen Energy* **1995**, *20*, 9−15.
(41) Kresse, G.; Furthmuller, J. Efficient iterative schemes for ab initio total-energy calculations using a plane-wave basis set. *Phys. Rev. B* **1996**, *54*, 11169−11186.
(42) Kresse, G.; Hafner, J. Norm-Conserving and Ultrasoft Pseudopotentials for First-Row and Transition-Elements. *J. Phys. Condens. Matter* **1994**, *6*, 8245−8257.
(43) Blochl, P. E. Projector Augmented-Wave Method. *Phys. Rev. B* **1994**, *50*, 17953−17979.
(44) Perdew, J. P.; Chevary, J. A.; Vosko, S. H.; Jackson, K. A.; Pederson, M. R.; Singh, D. J.; Fiolhais, C. Atoms, Molecules, Solids, and Surfaces - Applications of the Generalized Gradient Approximation for Exchange and Correlation. *Phys. Rev. B* **1992**, *46*, 6671−6687.
(45) Monkhorst, H. J.; Pack, J. D. Special Points for Brillouin-Zone Integrations. *Phys. Rev. B* **1976**, *13*, 5188−5192.
(46) Wu, Z. Y.; Karamad, M.; Yong, X.; Huang, Q. Z.; Cullen, D. A.; Zhu, P.; Xia, C. A.; Xiao, Q. F.; Shakouri, M.; Chen, F. Y.; Kim, J. Y.; Xia, Y.; Heck, K.; Hu, Y. F.; Wong, M. S.; Li, Q. L.; Gates, I.; Siahrostami, S.; Wang, H. T. Electrochemical ammonia synthesis via nitrate reduction on Fe single atom catalyst. *Nat. Commun.* **2021**, *12*, 2870.

https://doi.org/10.1021/acscatal.3c01088
ACS Catal. 2023, 13, 10560−10569